Journal of Geophysical Research Atmospheres

Supporting Information for

Prominent mid-latitude circulation signature in High Asia's surface climate during monsoon

Thomas Mölg[1], Fabien Maussion[2], Emily Collier[1], John C.H. Chiang[3], and Dieter Scherer[4]

[1]Climate System Research Group, Institute of Geography, Friedrich-Alexander-University Erlangen-Nürnberg (FAU), Germany, [2]Institute for Atmospheric & Cryospheric Sciences, University of Innsbruck, Austria, [3]Department of Geography & Center for Atmospheric Sciences, University of California, Berkeley, USA, [4]Chair of Climatology, Technische Universität Berlin, Germany.

Contents of this file

Overview

This supplementary material provides more details on the methods/data (Text S1, Text S2) and additional text that clarifies some results further (Text S3). The subsequent seven figures and four tables are based on the data introduced in the main paper and in Text S1. None of the items contains an independent new result not discussed in the study.

Text S1 – Methods: sources for reanalysis and other climate data

The American reanalysis is produced jointly by the National Centers for Environmental Prediction (NCEP) and the National Center for Atmospheric Research (NCAR). Data download was conducted at <*http://www.esrl.noaa.gov/psd/data/gridded/*> from the Earth System Research Laboratory (ESRL). The European reanalysis Era-Interim from the European Centre for Medium-Range Forecast (ECMWF) and MERRA (v2) from the National Aeronautics and Space Agency (NASA) represent products of the newer generation of reanalysis. Data were retrieved from the following sites: <*http://apps.ecmwf.int/datasets/data/interim-full-daily*> for Era-Interim and <*https://disc.sci.gsfc.nasa.gov/datareleases/merra_2_data_release*> for MERRA. A comparison of the main features of these three data sets can, for instance, be found in *Hofer et al.* [2015]. The higher spatial resolution of Era-Interim and MERRA is one major advantage, yet NCEP/NCAR reanalysis provides the longest records.

All-India rainfall is posted by the Indian Institute of Tropical Meteorology on their website (<*http://www.tropmet.res.in/*>). This widely-used Indian Summer Monsoon (ISM) index helped to perform the analysis in conjunction with Figure 8. One further data set complemented the material for the Supporting Information, which concerns the top-of-atmosphere outgoing longwave radiation (OLR). The National Oceanic and Atmospheric Administration (NOAA) provides global fields at 1° resolution since 1979, derived from radiance observations by both geostationary and polar orbiting satellites [*Lee, 2014*]. Data were also downloaded from the ESRL website above and included in the generation of Figure S7.

Text S2 – Methods: atmospheric modeling

Collier and Immerzeel [2015] modeled atmospheric dynamics at high spatial resolution for the Langtang catchment in the central Himalaya with the WRF model. In this location, a dedicated field experiment provided an unusually rich data set for the model evaluation. The authors demonstrated that with the set-up summarized in Table S2, it was possible to reproduce important characteristics of the observed near-surface air temperature and precipitation climate. Hence, we only modified the spatial domain (Figure S1) and horizontal grid spacing (20 km) for our needs, but maintained all other settings. We modeled the June-September season in the 1980-2014 period for every year with a W+ or W– case with consideration of spin-up time: every model run started on the simulation date 15th of May, and the first two weeks of model output were discarded. The starting year 1980 results from the first availability of the comparison data set (MERRA, v2).

It must be emphasized that usage of atmospheric model output in terms of absolute values requires a systematic evaluation [e.g., *Maussion et al., 2014; Gao and Xu, 2015*]. Here, the model output is intended for exploring basic patterns of differences (W+ minus W–) in the context of other data sources. The consistency of the WRF patterns with the widely used MERRA over wide areas of High Asia (Figure 5) provides one indication that the WRF simulation shows a useful degree of realism. In addition, the local anomalies from the mean (multi-decadal) spatial pattern for W+ and W– are reasonably well simulated with regard to the station data, for both seasons and for the two variables 2-m air temperature and precipitation (Table S4). All correlations are significant, and the root-mean-square-differences stay well within one standard deviation (σ) of the observations (only one case slightly exceeds 1 σ). We can therefore rule out a major bias in the model in terms of the seasonal climate anomalies.

Text S3 – Results: westerly influences in June

There are both similarities and one important difference to the results for JAS. The similarities concern the upper half of the troposphere. Figure S5 resembles in many respects the Figure 2 in the main paper, which suggests the atmospheric anomalies due to southward-shifted westerlies in June are also comprised of the dipole patterns found for JAS. A similar circulation anomaly with two centers provides again the dynamical basis (Figure S5c). The anomalies in Figure S5 are stronger than in Figure 2, but this is not unexpected since we are comparing a monthly mean with a three-month mean.

The important difference appears in the surface climate anomalies of June (Figure S6). Since there is obviously less agreement between the station data and the gridded data (MERRA and WRF) on the sign and distribution of these anomalies, distinct patterns as in JAS (Figure 5) are not recognizable. One possible interpretation is that there is a response time for the surface climate to adjust to the tropospheric forcing (the origin of the westerly-ISM interaction; see main paper), which could differ between the model-based data (MERRA and WRF) and reality. In general, it appears that the tropospheric anomalies (Figure S5) are portrayed more strongly in the model-based surface climate than in the station data (Figure S6).

The potential of lags and associated response times is well known for many climate processes, where the role of moist, deep convection was particularly emphasized for troposphere-surface coupling in tropical settings [*Chiang and Sobel, 2002*]. A closer look at the temporal pattern of convection for our case provides indeed a viable explanation (Figure S7). Compared to satellite observations, MERRA and WRF show a systematically stronger convection during June in all sectors of High Asia, which disappears towards the beginning of July. This pattern points to an artificially strong coupling of the near-surface layers and the upper troposphere in the model-based data for early summer. In JAS, however, the differences fluctuate more around the zero-line (and also have more time for compensation), which suggests more consistency between observations and model-based data in the coupling processes over the three-month window. A strong difference between June and JAS in the fraction of overlapping event years in the station and MERRA/WRF data does not apply and, hence, seems an unlikely explanation.

Additional references: supporting information only

Chiang, J. C. H., & Sobel, A. H. (2002). Tropical tropospheric temperature variations caused by ENSO and their influence on the remote tropical climate. *Journal of Climate*, *15*, 2616–2631. https://doi.org/10.1175/1520-0442(2002)015%3C2616:TTTVCB%3E2.0.CO;2

Gao, Y., & Xu, J. (2015). Evaluation of WRF mesoscale climate simulations over the Tibetan Plateau during 1979–2011. *Journal of Climate*, *28*, 2823–2841. https://doi.org/10.1175/JCLI-D-14-00300.1

Hofer, M., Marzeion, B., & Mölg, T. (2012). Comparing the skill of different reanalyses and their ensembles as predictors for daily air temperature on a glaciated mountain (Peru). *Climate Dynamics*, *39*, 1969–1980. https://doi.org/10.1007/s00382-012-1501-2

Lee, H. T. (2014). Climate Algorithm Theoretical Basis Document (C-ATBD): Outgoing longwave radiation (OLR)—Daily, NOAA's Climate Data Record (CDR) Program, CDRP-ATBD-0526.

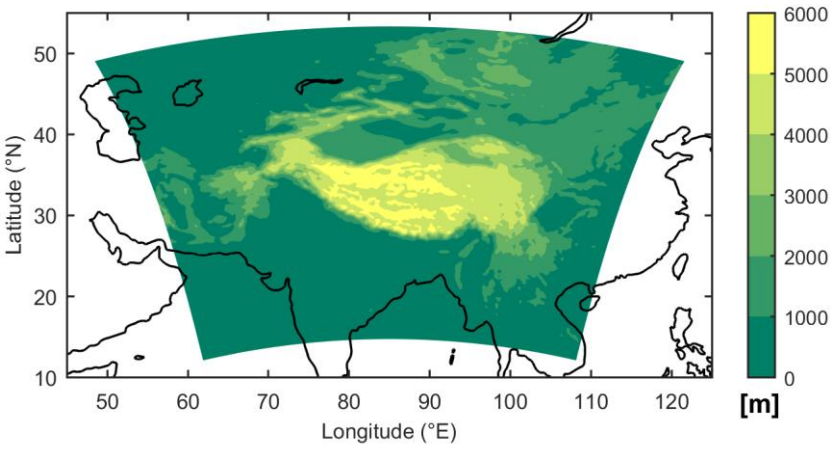

Figure S1. Atmospheric model domain. Extent and topographic height (meters above sea level) of the WRF model domain, which was configured with 20-km grid spacing and a Lambert conformal map projection.

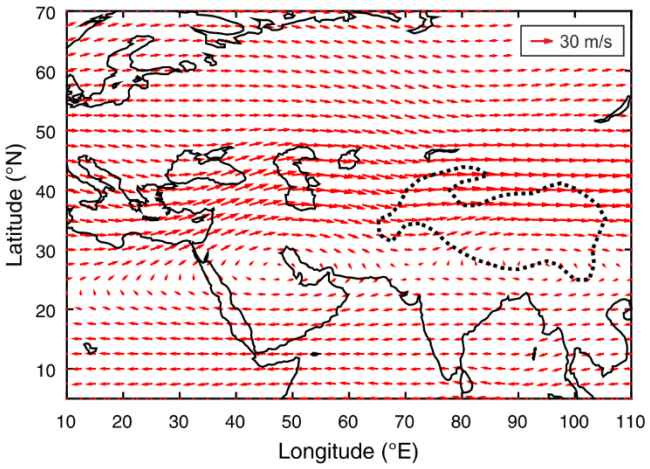

Figure S2. Upper tropospheric circulation. Mean wind vectors in JAS at 300 hPa, 1948-2014 (NCEP/NCAR reanalysis). Dashed line is the 2000-m isoline of terrain elevation, which roughly delineates High Asia.

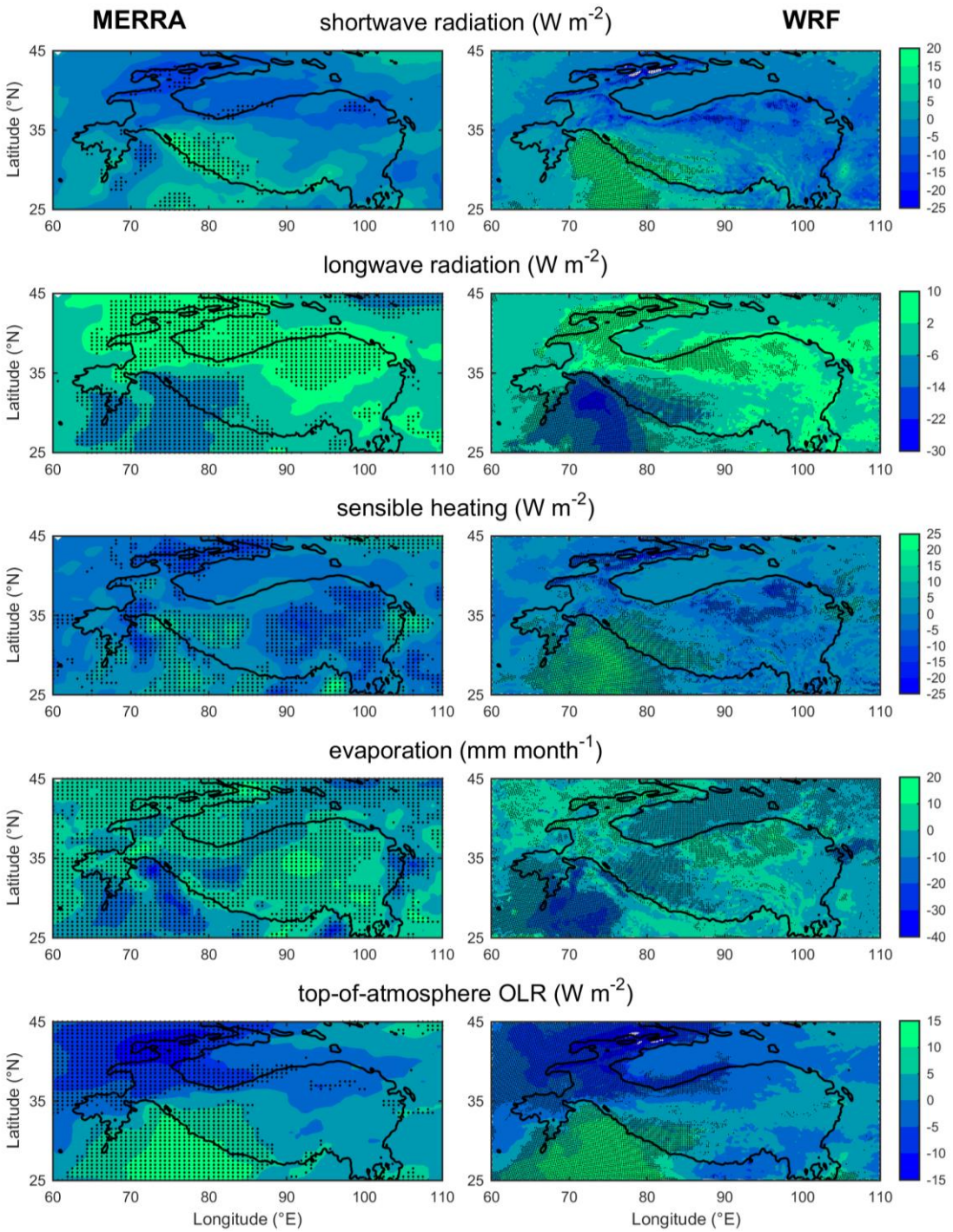

Figure S3. Energy budget processes. Differences between W+ and W– composites in the 1980-2014 period for JAS from the (left) MERRA and (right) atmospheric model (WRF) data: absorbed shortwave radiation, net longwave radiation, turbulent sensible heat flux (note that negative differences imply a stronger heat transfer from the surface to the atmospheric surface layer due to the sign convention), surface evaporation, and top-of-atmosphere outgoing longwave radiation (OLR). Dotted areas indicate significant differences at the FDR control level of 0.01 (due to the higher resolution in WRF and the resultant large number of grid points, the dots are smaller in the WRF plots). The bold line is the 2000-m contour from the WRF topography.

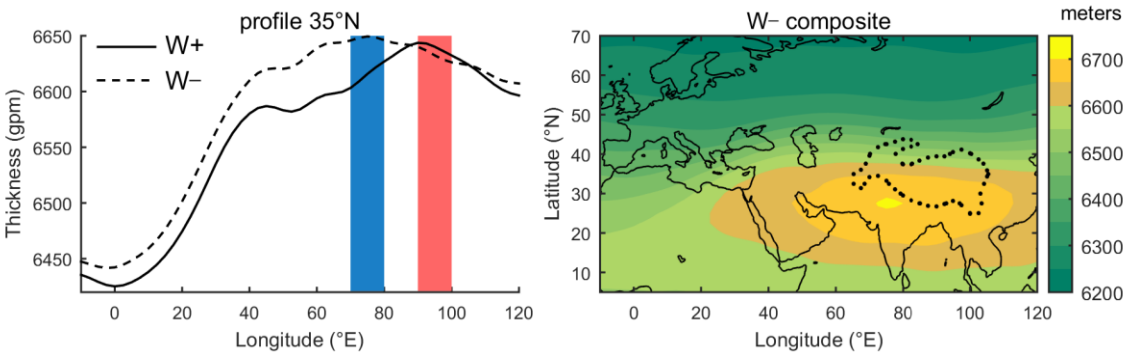

Figure S4. South Asian High in the upper half of the troposphere. Mean geopotential thickness of the 500-200 hPa layer in JAS, 1948-2014 (NCEP/NCAR reanalysis), (left) along 35° N for both phases and (right) for W– phases. The blue rectangle indicates the region of tropospheric and surface cooling in West High Asia during W+, red signifies the region of warming in East High Asia. The dashed bold line in the map is the 2000-m elevation contour and delineates High Asia.

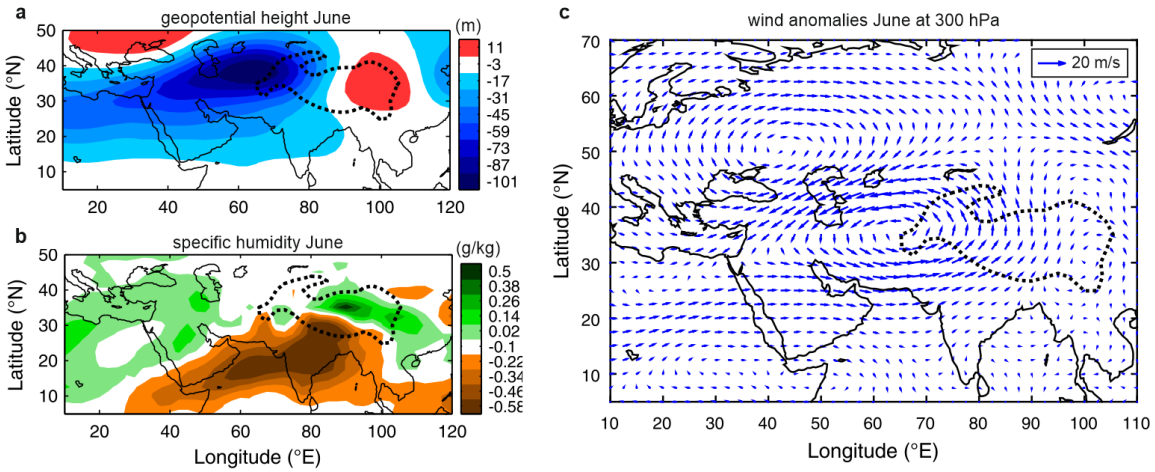

Figure S5. Same as Figure 2 in the article, but for June.

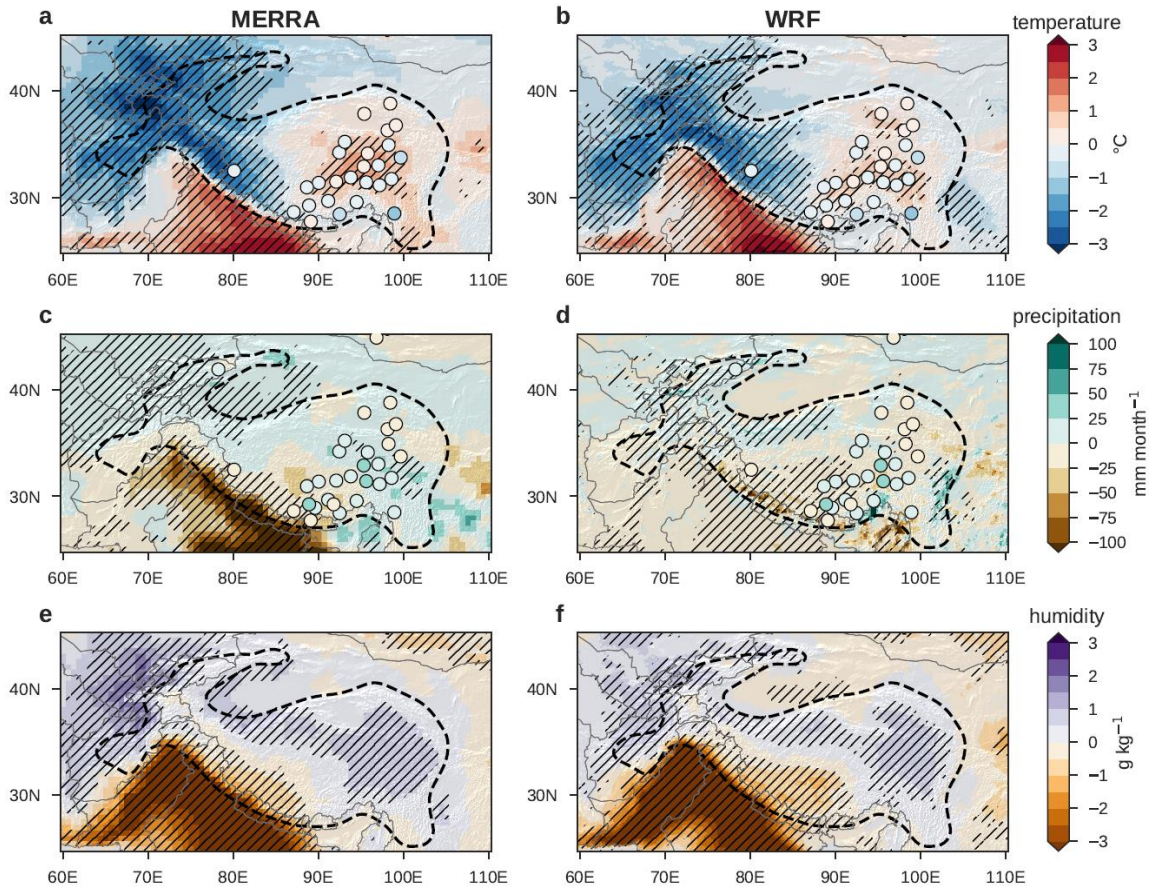

Figure S6. Same as Figure 5 in the article, but for June.

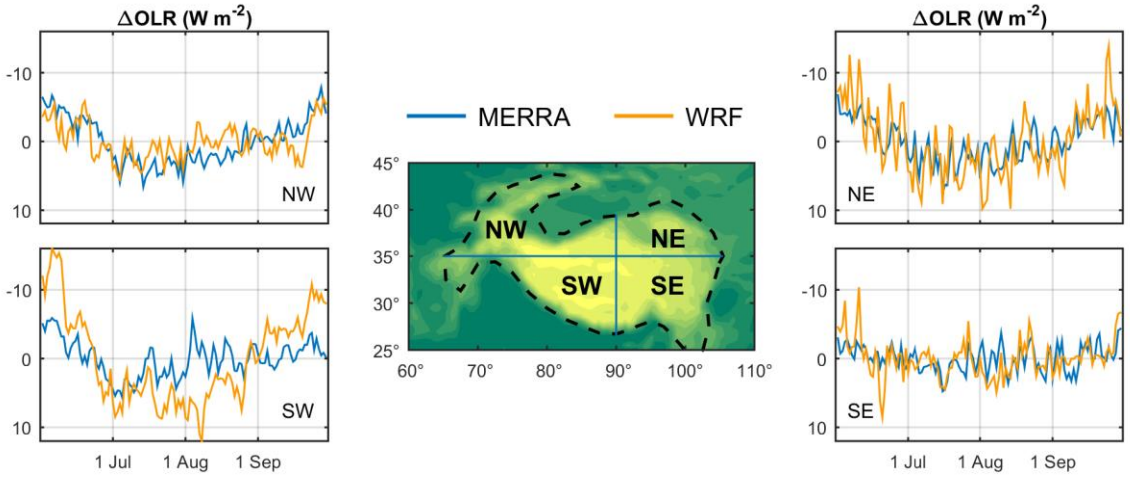

Figure S7. Convection in the JJAS season. Differences in mean daily top-of-atmosphere OLR in different sectors of High Asia (MERRA or WRF minus NOAA-satellite OLR) from 1 June to 30 September. Time series are constructed from daily values averaged for all W+ and W– cases in the 1980-2014 period. Differences are calculated from the normalized time series to remove the effect of systematic biases. The map sketch shows the sector definitions: only grid cells > 2000 m above sea level (dashed contour) are considered, and the 90°E meridian and 35°N latitude circle serve as divides. Note that all y-axes are reversed since lower OLR indicates stronger convection.

	June			JAS		
	1	2	3	1	2	3
Retop	0.64 (44)	0.61 (35)		*0.30* (58)	0.87 (24)	
Shumint		0.77 (18)			0.69 (15)	
U300	0.74 (43)			0.52 (40)	*0.40* (22)	**0.33** (16)
V300	0.70 (39)			0.70 (38)		**M**

bold: significant correlations with westerly index only
M: significant correlations with monsoon index only
normal: significant correlations with westerly and monsoon index, but westerly correlation stronger
italics: significant correlations with westerly and monsoon index, but monsoon correlation stronger

Table S1. **Circulations and variability patterns**. Correlation coefficients between the westerly index (Figure 1) and the time series of the three leading EOFs of four different atmospheric variables in the Figure 3 domain (25°-45°N, 60°-110°E) for June and JAS, 1948-2014. Only correlations significant at the 1% level are shown. Numbers in parentheses show the percentage of total-field variance explained by the respective EOF. Retop is the geopotential thickness of the 500-200 hPa layer, Shumint is the vertically-integrated specific humidity of the 500-300 hPa layer, and U300 and V300 are the zonal and meridional wind components at 300 hPa, respectively; rotated EOFs for Shumit (see article text). All correlation coefficients are shown positive, since sign differences cannot be interpreted without the spatial EOF pattern. The font style and the entry "M" reveal the comparison with the correlations of the EOFs to the monsoon index (see sub-caption).

Component	Setting
discretization	
grid dimension and spacing	269 × 219, 20 km
levels in vertical	50
model top pressure	50 hPa
lateral boundary conditions	Era-Interim, 6 hourly forcing
model physics	
radiation	CAM
microphysics	Morrison
cumulus parameterization	Kain-Fritsch
planetary boundary layer	MYNN level 2.5
atmospheric surface layer	Monin-Obukhov (revised MM5)
land surface scheme	Noah-MP
diffusion	physical space
top boundary condition	Rayleigh damping

Table S2. WRF configuration. Main settings for discretization and model physics. For further details and references of the schemes or parameterizations see *Collier and Immerzeel* [2015].

	Lon. (°E)	Lat. (°N)	First Year	Last Year	Available W+ (W–) seasons, prec.		Available W+ (W–) seasons, temp.	
					June	JAS	June	JAS
Bange	90.02	31.38	1957	1990	10 (4)	10 (5)		
Baingoin	90.02	31.37	1957	1990			9 (5)	9 (4)
Changdu	97.17	31.15	1953	2013	11 (6)	11 (6)		
Da Quidam	95.37	37.85	1957	1990	10 (5)	10 (5)	10 (4)	10 (4)
Darlag	99.65	33.75	1957	2013	10 (5)	10 (5)	9 (6)	9 (6)
Dege	98.57	31.73	1957	1990	10 (5)	10 (5)	10 (4)	10 (4)
Dengqen	95.60	31.42	1957	1990	9 (3)	9 (4)	9 (3)	9 (4)
Deqen	98.90	28.50	1953	2013	10 (6)	10 (6)	9 (6)	9 (6)
Dulan	98.10	36.30	1957	2013	12 (6)	12 (6)	12 (6)	12 (6)
Jiangzi	89.60	28.92	1957	1990	10 (5)	10 (4)		
Lhasa	91.13	29.67	1953	2013	11 (6)	11 (6)	9 (7)	9 (7)
Lhunze	92.47	28.42	1959	1990	9 (4)	9 (5)	8 (4)	8 (5)
Madoi	98.22	34.92	1953	1990	10 (6)	10 (6)	10 (6)	10 (6)
Station G	96.80	44.90	1962	1983	9 (2)	9 (2)		
Nagqu	92.07	31.48	1957	1990	10 (5)	10 (5)	8 (4)	8 (4)
Naidongz	91.77	29.25	1957	1990	10 (5)	10 (4)		
Nyingchi	94.47	29.57	1953	1990	10 (6)	10 (5)	9 (4)	9 (4)
Pagri	89.08	27.73	1957	1990	10 (5)	10 (4)		
Qilian Tuole	98.42	38.80	1957	1990	10 (5)	10 (5)	10 (4)	10 (4)
Qumarleb	95.78	34.13	1957	1990	10 (5)	10 (5)	10 (5)	9 (5)
Rikaze	88.88	29.25	1957	1990	10 (5)	10 (5)		
Shiquanhe	80.08	32.50	1962	2013	8 (4)	9 (3)	7 (3)	7 (2)
Sog Xian	93.78	31.88	1957	2013	10 (5)	10 (4)	9 (6)	9 (5)
Tingri	87.08	28.63	1959	1990	9 (5)	8 (5)	8 (3)	7 (3)
Tuotuohe	92.43	34.22	1957	2013	10 (5)	10 (5)	9 (6)	9 (6)
Tyan Shan	78.23	41.92	1953	1990	8 (6)	8 (6)		
Uulan Caka	99.08	36.78	1957	1990	10 (5)	10 (5)	10 (4)	10 (3)
Wudaoliang	93.08	35.22	1957	1990	10 (5)	10 (5)	9 (5)	9 (5)
Xainza	88.63	30.95	1962	2013	9 (4)	9 (4)	9 (5)	9 (4)
Xigaze	88.88	29.25	1957	1990			10 (3)	10 (3)
Yushu	97.02	33.02	1953	2013	10 (6)	10 (6)	11 (7)	11 (6)
Zadoi	95.30	32.90	1957	1990	10 (5)	10 (5)	9 (5)	10 (5)

Table S3. Meteorological station data. Characteristics of the publically-available station data in the study area (source: KNMI climate explorer). Station data were scanned for all available W+ and W– seasons since 1948 (Figure 1). The first and last year of the resultant records (in any variable and season) are also given; however, this does not imply uninterrupted records. No entries indicate missing data.

	Temperature				Precipitation			
	W+ June	W– June	W+ JAS	W– JAS	W+ June	W– June	W+ JAS	W– JAS
r	0.72**	0.70**	0.70**	0.70**	0.54**	0.59**	0.38*	0.50**
RMSD	2.4	2.5	2.1	2.2	35	31	34	27
STD	3.4	3.6	3.0	3.2	42	36	33	28

Table S4. Model and observations. Spatial correlation of mean seasonal anomalies in June and JAS for 2-m air temperature (K) and precipitation (mm month^{-1}) during W+ and W– phases between observations (Table S3) and WRF model results. The correlation coefficients (*r*) are significant at 0.05 (*) or 0.01 (**). RMSD is the root-mean-square difference between observations and model, STD is the standard deviation in observations (both in the respective units). Note that the mean value for each location stems from different years in the observation and the model (cf. Table S3 and Section 2.3 in the main paper). The locations in the model are determined by cubic spline interpolation.